Towards the low-dose characterization of beam sensitive nanostructures via implementation of sparse image acquisition in scanning transmission electron microscopy

2017 Meas. Sci. Technol. 28 045402

(http://iopscience.iop.org/0957-0233/28/4/045402)

IOP Publishing Measurement Science and Technology
Meas. Sci. Technol. **28** (2017) 045402 (9pp) doi:10.1088/1361-6501/aa57df

Towards the low-dose characterization of beam sensitive nanostructures via implementation of sparse image acquisition in scanning transmission electron microscopy

Sunghwan Hwang[1], Chang Wan Han[1], Singanallur V Venkatakrishnan[2], Charles A Bouman[2] and Volkan Ortalan[1]

[1] School of Materials Engineering and Birck Nanotechnology Center, Purdue University, West Lafayette, IN, United States of America
[2] School of Electrical and Computer Engineering, Purdue University, West Lafayette, IN, United States of America

E-mail: vortalan@purdue.edu

Received 23 August 2016, revised 19 December 2016
Accepted for publication 9 January 2017
Published 10 February 2017

Abstract

Scanning transmission electron microscopy (STEM) has been successfully utilized to investigate atomic structure and chemistry of materials with atomic resolution. However, STEM's focused electron probe with a high current density causes the electron beam damages including radiolysis and knock-on damage when the focused probe is exposed onto the electron-beam sensitive materials. Therefore, it is highly desirable to decrease the electron dose used in STEM for the investigation of biological/organic molecules, soft materials and nanomaterials in general. With the recent emergence of novel sparse signal processing theories, such as compressive sensing and model-based iterative reconstruction, possibilities of operating STEM under a sparse acquisition scheme to reduce the electron dose have been opened up. In this paper, we report our recent approach to implement a sparse acquisition in STEM mode executed by a random sparse-scan and a signal processing algorithm called model-based iterative reconstruction (MBIR). In this method, a small portion, such as 5% of randomly chosen unit sampling areas (i.e. electron probe positions), which corresponds to pixels of a STEM image, within the region of interest (ROI) of the specimen are scanned with an electron probe to obtain a sparse image. Sparse images are then reconstructed using the MBIR inpainting algorithm to produce an image of the specimen at the original resolution that is consistent with an image obtained using conventional scanning methods. Experimental results for down to 5% sampling show consistency with the full STEM image acquired by the conventional scanning method. Although, practical limitations of the conventional STEM instruments, such as internal delays of the STEM control electronics and the continuous electron gun emission, currently hinder to achieve the full potential of the sparse acquisition STEM in realizing the low dose imaging condition required for the investigation of beam-sensitive materials, the results obtained in our experiments demonstrate the sparse acquisition STEM imaging is potentially capable of reducing the electron dose by at least 20 times expanding the frontiers of our characterization capabilities for investigation of biological/organic molecules, polymers, soft materials and nanostructures in general.

Keywords: scanning transmission electron microscopy (STEM), compressive sensing, low dose imaging, beam sensitive materials, image inpainting, model based image reconstruction (MBIR), characterization of soft materials

(Some figures may appear in colour only in the online journal)

1. Introduction

Since Albert Crewe's pioneering works on scanning transmission electron microscopy (STEM) [1–4], modern STEM has been one of the mainstream techniques for high-resolution characterization of various materials at the nanoscale. Specifically, with the recent development of the aberration correctors for electron probe-forming lenses and the field emission gun (FEG) having high coherency and brightness, sub-angstrom resolution imaging with a substantially increased signal-to-noise ratio (SNR) has been realized [5, 6]. Along with its atomic spatial resolution, aberration-corrected STEM equipped with spectrometers including electron energy loss spectroscopy and x-ray energy dispersive spectroscopy has been successfully demonstrated its capability of chemical analysis with single atomic sensitivity [7, 8].

In recent years, along with the remarkable advancements in STEM in terms of its hardware, researchers' attention has also been paid to the STEM probe control protocol and/or image acquisition algorithm. Sang and LeBeau [9] demonstrated that drift image distortion could be successfully removed by performing a series of fast-acquisitions of images with rotating the scan coordinate system between successive acquisitions. In addition to the efforts reducing the scan-distortion artifacts, the possibility of the low dose imaging in STEM has also been investigated by Buban *et al* where they investigated the feasibility of the STEM approach based on a fast raster scan and a low probe current for low dose imaging [10].

Recently, new sparse signal processing theories, such as compressive sensing (CS) [11] and model-based iterative reconstruction (MBIR) [12], that allow to reconstruct an original signal from a sparsely acquired one, have been emerged into the field of electron microscopy and those theories opened a new possibility for STEM to be operated within the scheme of sparse sampling theories. The last few decades have seen significant progress in the design of algorithms that can reconstruct an image from a sparse set of measurements. While the Nyquist sampling criteria guarantees perfect signal reconstruction when the sampling rate is at least twice the maximum signal frequency, it is possible to reconstruct a signal from far fewer measurements if we can exploit some *a priori* information about the signal. This is particularly true in the case of images that have local and non-local correlations and hence are generally sparse in some basis. One such class of image reconstruction algorithms, termed as MBIR, casts the reconstruction of an unknown image from noisy measurements in a probabilistic framework that exploits information about the noise statistics in the measurement, the physics of data formation and low dimensional models for the image. Often such modeling results in the reconstruction being cast as an optimization problem where we find the reconstruction that best matches the data while being constrained by the assumptions of the image model.

Recent theoretical results from the field of CS have further enhanced interest in the area of MBIR methods. Midgley research group has demonstrated that CS is applicable to STEM electron tomography [13–15]. Furthermore, Binev and coworkers have discussed the possibility of exploiting the sparsity of images in a wavelet basis to perform sparse image reconstruction for STEM [16]. Stevens *et al*, conceptually proposed a CS STEM image acquisition strategy in which STEM images are acquired not by conventional raster scan but by the random subsampled scan and sparsely acquired images are recovered via Bayesian dictionary learning [17]. Although it requires hardware modifications, Béché *et al*, experimentally demonstrated that the fast electromagnetic electron deflection synchronized with continuous raster scan in STEM allows CS imaging [18].

As an effort to implement a sparse acquisition scheme in STEM with no hardware modification, we propose a STEM technique operated by a non-raster scan method, so called the random sparse-scan. We report the first experimental results obtained with the random sparse scan STEM technique implemented on a widely used conventional microscope, an FEI Titan 80-300 S/TEM and discussed the potential of this technique towards a low dose STEM imaging of beam sensitive nanomaterials.

2. Methods

The random sparse-scan STEM (SSTEM will be used in what follows) technique is mainly comprised of a non-raster scan based image acquisition followed by an image inpainting process to reconstruct the fully sampled image from a subsampled one. Figure 1 describes the process flow of the method for acquiring a subsampled image and image reconstruction. The image acquisition is performed utilizing a high angle annular dark field (HAADF) detector with conventional STEM alignments. The ROI of a specimen is expressed as an array of 'discrete' unit sampling areas (figures 1(b) and (d).

As in conventional HAADF-STEM, incoherently scattered electrons are collected by a HAADF detector during dwelling of electron probe onto a unit sampling area. Although the collection of the signals using a HAADF detector is the same as that for a conventional detector, the electron probe positioning scheme is entirely different. Figure 1(d) illustrates the random SSTEM image acquisition protocol. In conventional STEM, the signal is continuously collected from each 'unit sampling area' of the ROI by a continuous raster scan (figure 1(b)).

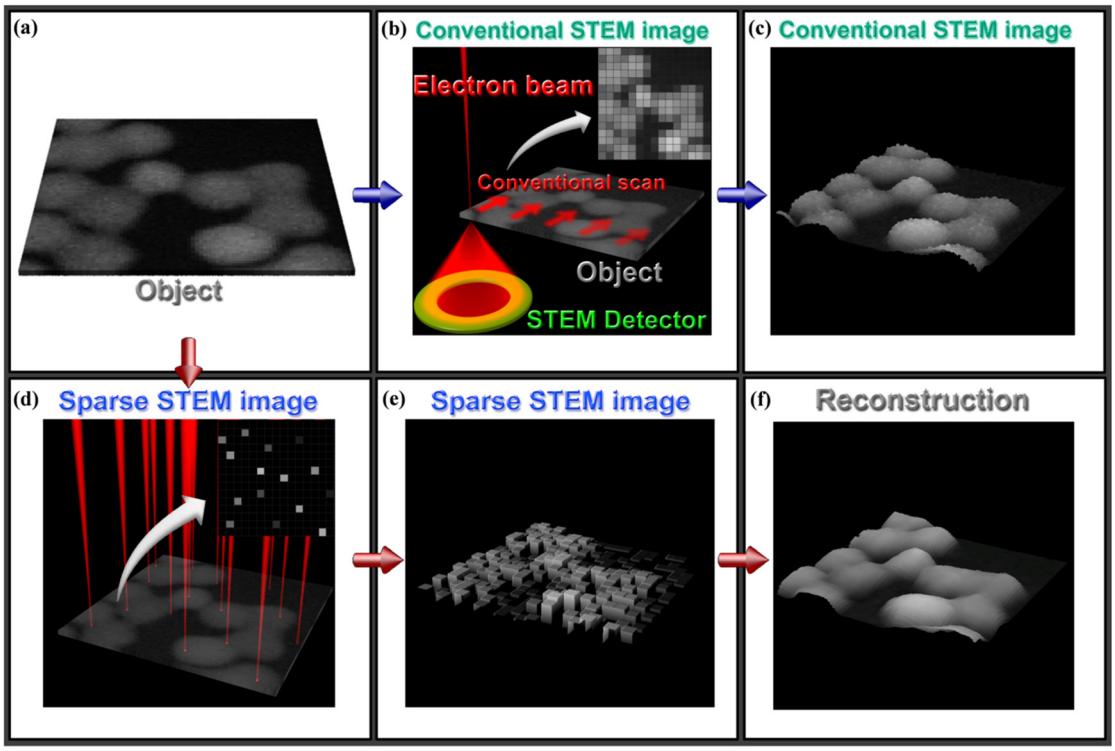

Figure 1. Illustration of the process flow of the sparse acquisition STEM technique. (a) Object for the conventional or random sparse scan (here, gold nanoparticles on amorphous carbon film). (b) Continuous raster scan in the conventional STEM. (c) The 3D intensity surface plot of the acquired conventional STEM image. (d) Discontinuous random sparse scan (e) The 3D intensity surface plot of the sparsely collected STEM image. (f) 3D intensity surface plot of the reconstructed image from the sparsely acquired STEM image.

The 'unit sampling area' means a discrete area on the sample, which corresponds to a single pixel of a STEM image.

In contrast to a conventional STEM, only a small number of unit sampling areas, which is determined by the predefined sampling ratio, are randomly chosen and exposed to the electron probe during the random sparse-scan (figure 1(d)), and therefore, the image having intensities of randomly chosen unit sampling areas is acquired as illustrated in figure 1(e). During the sparse-scan process, the electron probe is positioned to stay on the randomly selected unit sampling areas for a certain dwell time and then repositioned to the probe parking position, which is a predetermined position away from the region of interest of the sample. This process is repeated until the total number of the scanned unit sampling area satisfies the predefined sampling ratio. To implement the sparse-scan of the electron probe, TEM imaging and analysis software (TIA) scripting was utilized on an FEI Titan 80-300 S/TEM. Then, the sparsely acquired image (figure 1(e)) is used to reconstruct the full image (figure 1(f)) by the MBIR based image-inpainting algorithm—termed Plug-and-Play priors [19]. As the specimen for the sparse acquisition experiments, Au nanoparticles deposited on holey carbon film is chosen to demonstrate the resolution capabilities of SSTEM. More detailed description on the process flow of sparse acquisition using TIA scripting is described in the following section.

2.1. Acquisition of sparse STEM images

We designed a random sparse scanning application (*SSTEMbot*) which employs a custom automation interface supported by the TIA. The automation interface enabled us to control the electron probe in a custom manner without any hardware modification: First, experimental parameters, such as digital image resolution, dwell time, and sampling ratio are preset. Second, a matrix corresponding to the predefined digital image resolution is prepared to store the intensities collected from each unit sampling areas (these unit sampling areas of a sample correspond to pixels in a STEM image). Third, portion of the matrix elements are randomly chosen according to the sampling ratio, and the locations of the chosen matrix elements define the positions of the unit sampling areas at which the electron probe is positioned. Fourth, the *SSTEMbot* begins to examine each unit sampling area and stores the integrated intensity value for the corresponding pixel of the image matrix. Then, the STEM probe is moved to the predefined parking position. The *SSTEMbot* continues to reposition the electron probe to another unit sampling area until all the randomly selected unit sampling areas are examined. Figure 2 shows the sparse image which is acquired by the *SSTEMbot*.

In the figure, the 20% sampled image is compared to the 100% sampled one (figures 2(a) and (b)). Figures 2(c) and (d) illustrates the details of the images acquired conventionally

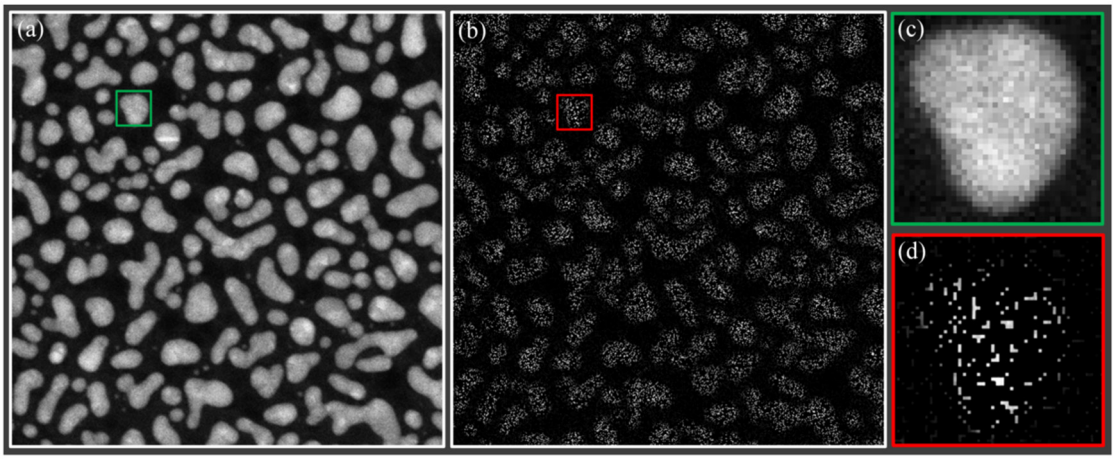

Figure 2. Example of a sparse acquisition STEM image. (a) 100% sampled conventional STEM image. (b) 20% sampled image from the random sparse-scan. The location of the green and red boxes in (a) and (b) are magnified to show the details of the images. (c) The magnified image of the area highlighted with the green box in the 100% sampled STEM image. (d) The magnified image of the area highlighted with the red box in the 20% sampled STEM image. Only 20% of pixels have the intensity values while the rest are skipped during scanning and remain black with zero intensity.

and sparsely showing a small magnified section from the same areas of the 100% and 20% sampled images, respectively. As an example, the experimental parameters for 1% sub-samples image are 0.24 μs dwell time, 0.114 s unit sampling area collection time and 755 s total run time of the program. The average time to collect a unit sampling area, which does not change with sampling, includes probe parking time, time delay between scan/check commands in the SSTEMbot code, time for while loop to check the end of scan, the time to calculate the time interval to collect a unit sampling area, the time for actual execution of the process by TEM, and the dwell time. For high sampling ratios, we also implemented an optional drift correction algorithm into the SSTEMbot. The total run time also includes additional processing times for separate functions running in the code during collection, such as preparation parameters to scan, calculation and define region to scan, etc. Therefore, improving the speed of the communication between the software (TIA) and the hardware of the current conventional STEM instruments is critical to reduce these internal delays and to achieve full potential of the sparse collection strategy in low dose imaging.

2.2. Reconstruction algorithm

We used the MBIR [20] approach to reconstruct the image from the sparse set of measurements. MBIR is a powerful framework for solving reconstruction and other inverse problems in imaging. Along with modeling the physics of image formation, and the noise in the image, these methods allow for the incorporation of models for the image (prior model), enabling significant improvements in image quality in a variety of applications [21–23].

In MBIR, a statistical model for the image is combined with a statistical model for the image to formulate the reconstruction as solving an estimation problem. In particular, if y is the measured image organized as a $M \times 1$ vector and x is the underlying image to be reconstructed organized as a $N \times 1$ vector, we will require a description of $p(y|x)$, the probability density function of the measured image given the unknown (forward model) and a description of $p(x)$, the probability density function of the unknown image (prior model). Given these probabilistic formulations, the reconstruction is typically given by the maximum *a posteriori* probability (MAP) estimate, which using Baye's rule can be expressed as,

$$\begin{aligned} \hat{x} &= \arg\min_x \{-\log p(y|x) - \log p(x)\} \\ \hat{x} &= \arg\min_x \{l(y;x) + \beta s(x)\} \end{aligned} \tag{1}$$

where $l(y;x)$ is the log-likelihood function, $s(x)$ is the log-prior function and β is a parameter used to adjust the relative weights between the two models. We also emphasize that the formulation of the models determines the quality of the reconstruction while the specific choice of optimization affects the speed of reconstruction. At this stage, MBIR can simply viewed as finding the value that best matches the data while being constrained by the prior model. MBIR methods typically tradeoff bias (resolution) for variance (noise) in order to produce a reconstruction. Thus, a higher bias introduced via the prior model can blur details in the images while lowering the noise variance. However, compared to conventional methods they tend to have a lower error in the sense of balancing the noise v/s resolution tradeoff.

While it is possible to formulate the forward model based on knowledge of the physics of the acquisition and the noise characteristics of the detector, formulation of a prior model for images requires accurately modeling the ensemble behavior of the image to be acquired. The choice of the prior model can help to significantly improve image quality as demonstrated by the recent success of various image denoising algorithms [24–29]. However, extending these models to other applications has been challenging in general. The Plug-and-Play (P&P) priors framework, inspired by the ADMM algorithm [30] for solving equation (1) under certain conditions, provides a method to easily integrate a wide variety of

Set the value of parameters λ and σ_n^2

Initialize $v = x,\ u = 0$

Repeat until convergence{

1. $\tilde{x} = \hat{v} - u$

$$\hat{x} \leftarrow \left(\frac{1}{\sigma_w^2}A^tA + \lambda I\right)^{-1}\left(\frac{1}{\sigma_w^2}A^ty + \lambda\tilde{x}\right)$$ //Invert foward model

2. $\tilde{v} = \hat{x} + u$

$\hat{v} \leftarrow H_{BM\,3D}\left(\tilde{v};\sigma_n^2\right)$ //Denoise $\tilde{v}$

3. $u \leftarrow u + \left(\hat{x} - \hat{v}\right)$

}

Figure 3. Plug-and-Play algorithm used for the STEM inpainting problem. The algorithm alternates between a model inversion and a denoising step. The prior model only influences the denoising step of the algorithm.

sophisticated prior models (image constraints) into the MBIR framework by implicitly defining them via image denoising algorithms. In short, the ADMM framework involves repeated application of the following steps until convergence:

1. $\hat{x} \leftarrow \arg\min_x \left\{ l(y;x) + \frac{\lambda}{2}\|x - \hat{\nu} + u\|_2^2 \right\}$ //Invert forward model
2. $\hat{\nu} \leftarrow \arg\min_\nu \left\{ \frac{\lambda}{2\beta}\|\hat{x} + u - \nu\|_2^2 + s(\nu) \right\}$ //Denoise $\hat{x} + u$
3. $u \leftarrow u + (\hat{x} - \hat{\nu})$

where λ is a parameter of the algorithm. Notice that the second step is a denoising operation that only depends on the choice of prior model. We define this denoising operator for a specific prior model to be given by

$$H(y;\sigma_n^2) = \arg\min_x \left\{ \frac{1}{2\sigma_n^2}\|y - x\|_2^2 + s(x) \right\}. \quad (2)$$

If we define the forward model inversion operator as

$$F(y,\tilde{x};\lambda) = \arg\min_x \left\{ l(y;x) + \frac{\lambda}{2}\|x - \tilde{x}\|_2^2 \right\}. \quad (3)$$

then the Plug-and-Play priors algorithm for any image model implemented via a denoising operator, H, is given by repeating the following steps until convergence

1. $\tilde{x} = \hat{\nu} - u$
   $\hat{x} \leftarrow F(y,\tilde{x};\lambda)$ //Invert forward model
2. $\tilde{\nu} = \hat{x} + u$
   $\hat{\nu} \leftarrow H(\tilde{\nu};\sigma_n^2)$ //Denoise $\tilde{\nu}$ based on desired prior; $\sigma_n^2 = \frac{\beta}{\lambda}$
3. $u \leftarrow u + (\hat{x} - \hat{\nu})$

Thus, the Plug-and-Play method provides a flexible framework that allows state-of-the-art forward models of imaging systems to be matched with state-of-the-art prior or denoising models in the MBIR framework [19, 31].

Next, we apply the above Plug-and-Play framework for the STEM sparse reconstruction problem. We model each measurement as the sum of the pixel value and zero mean Gaussian noise with standard deviation σ_w. If A is a $M \times N$ binary matrix which maps the underlying image to the measurements, then we model each measurement y_i as

$$y_i = (Ax)_i + w_i$$

where $(Ax)_i$ is the ith element of the vector Ax, w_i is a zero mean Gaussian random variable with variance σ_w^2. This results in $l(y;x) = \frac{1}{2\sigma_w^2}\|y - Ax\|_2^2$. Using this model we can compute the forward model inversion operator $F(y,\tilde{x};\lambda)$ in (3) to be $\left[\frac{1}{\sigma_w^2}A^tA + \lambda I\right]^{-1}[A^ty + \lambda\tilde{x}]$. We note that for sufficiently large number of counts, the Gaussian assumptions are reasonable, while for the low-dose case this model can easily be replaced by a Poisson model. We choose the BM3D [28] filter for the denoising operator H. The BM3D denoising algorithm works by finding similar patches in the image, transforming them into a new basis, zeroing out the small coefficients and then applying an inverse transform to obtain the denoised patches. The BM3D filter has been shown to be very effective in the case of denoising natural images. Furthermore, the BM3D is a non-iterative method resulting in a fast implementation for the inpainting problem. Using these models our STEM image reconstruction method is summarized in figure 3.

3. Results and discussion

Figure 4 shows the results of image inpainting from sparsely acquired STEM images of Au nanoparticles on holey carbon film. 100% sampled (conventional STEM) image is shown in figure 2(a). First, second, and third columns are sparsely sampled (upper row) and reconstructed (bottom row) images with the sampling ratio of 10%, 5%, and 3%, respectively. The reconstructed image from the 10% sampled image shows high consistency with the conventional image in terms of the morphology of each particle, edge sharpness, and contrast variation between or within particles (figure 4(d)). For 5% sampling and reconstruction, although the edge of each

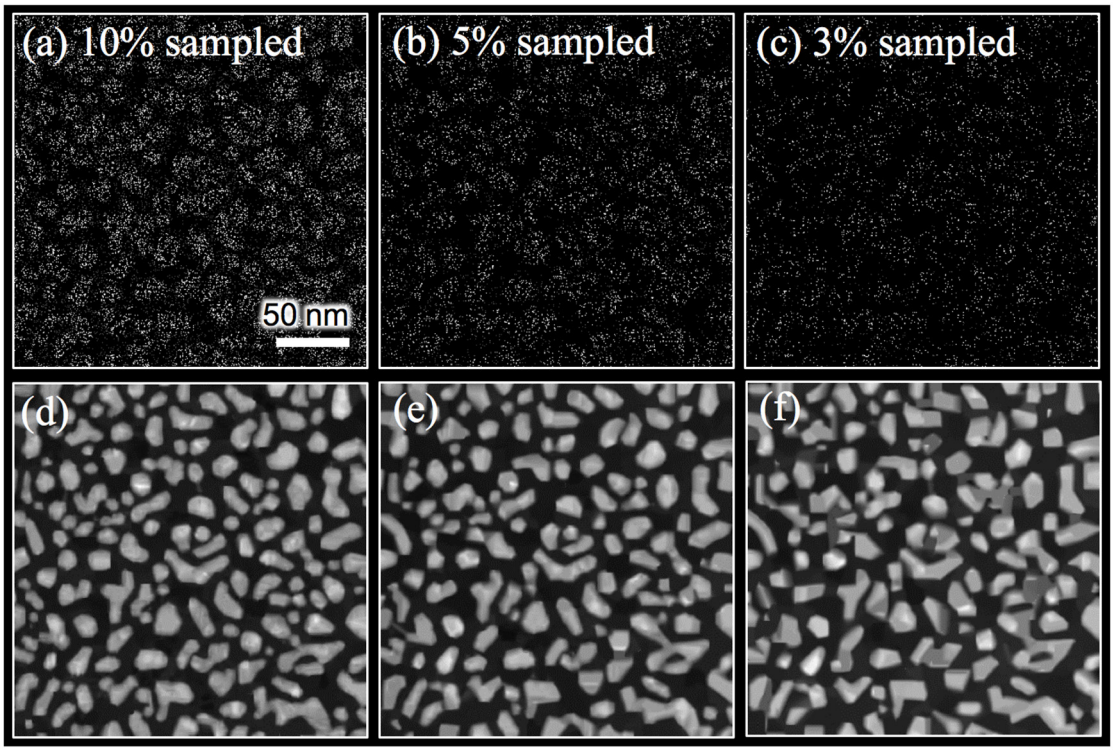

Figure 4. Random sparse images and their reconstructions. (a)–(c) Are the random sparse images with the sampling ratio of 10, 5, and 3%, respectively. The reconstructions from the 10, 5, and, 3% sampled images are shown in (d)– (f), respectively.

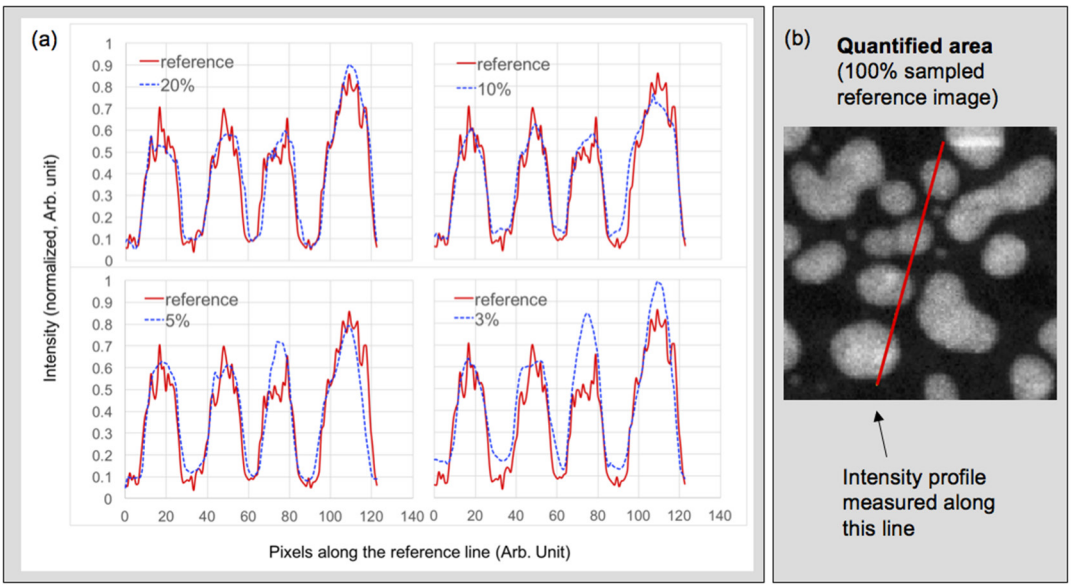

Figure 5. Comparison of the measured intensity profiles along the line from the reference (100% sampled image) and those reconstructed from the 20%, 10%, 5%, and 3% subsampled images. (a) Measured intensity profiles (solid line: 100% sampled, broken line: subsampled) along the red line marked on the inset image. (b) STEM image showing the location where intensity profiles were measured.

particle is blurred compared to the conventional image, the morphologies and the contrast of particles are still consistent with the conventional one (figure 4(e)). The rightmost image reconstructed from the most sparsely acquired (3% sampling) starts losing the details of the original image (figure 4(f)). The contrast variation, which is shown in the conventional image, is somewhat suppressed and the edges of the particles are further blurred.

In order to evaluate the quality of the reconstructed images, intensity profiles along the red line shown in figure 5(b) were also measured both from 100% sampled (reference) image and from the reconstructed images with 20%, 10%, 5%, and 3% sampling ratio as shown in figure 5. As can be seen, the normalized profiles down to 10% are remarkably consistent with the profile taken from the reference image. The profiles taken from the 5% and 3% sampled images show some

differences in terms of the intensities, however, the measured particle size by the reference line are still consistent with the reference image. This indicates that the shape and size of electron beam sensitive specimens, such as viruses, proteins and small metal nanoclusters/nanoparticles can still be identified even with the 3% subsampling.

We also quantified other parameters, such as average diameter and the number of the gold particles from the conventional STEM image and the reconstructed images to compare the effect of the sampling ratio in quantitative analysis. Table 1 illustrates the number of particles and average diameter of particles in the reference (conventional STEM image) and the reconstructed images from sparsely scanned images.

Particles smaller than 3 nm were excluded for this study because the contrast of those small particles was not sufficient to identify them in the selected magnification. The results from the 20%, 10%, and 5% sampled images show very high consistency with the reference with respect to both the average diameter and the number of particles. In the case of the number of particles, 20%, 10%, and 5% sampling show almost the same value (~150) to that of the reference. As for the average diameter of the particles, the values of the reference, 20%, and 10% sampled images are also equivalent to each other up to one place of decimals, and the difference between the reference and 5% sampling is only about 2%. It is noteworthy that even the 3% sampled image can estimate the diameter of particles with precision of about 95%. Moreover, further improvement can be obtained through the optimization of the reconstruction algorithm by adapting an online strategy for reconstruction—instead of reconstructing the images offline. If what we learn about the image during acquisition is incorporated into the reconstruction algorithm in real time, we can optimize the acquisition to focus on the important areas of the image for more reliable quantitative analysis [32].

To quantitatively discuss the effect of the reconstruction with varying sampling ratio, peak signal-to-noise ratios (PSNR), which is a quality metric evaluating the image processing result, were calculated, where we used the fully sampled image as the ground-truth. PSNR is defined with the following equation:

$$\mathrm{PSNR} = 10\log_{10}\left(\frac{R^2}{\mathrm{MSE}}\right)$$

$$\mathrm{MSE} = \frac{\sum_{M,N}[I_1(m,n) - I_2(m,n)]^2}{M \times N}$$

where MSE, I, M, and N are the mean squared error, the pixel intensity of an image, the number of rows and columns in the images, respectively. I_1, I_2 and R are the reference (fully sampled) image, the reconstructed image and the maximum possible pixel value of the image, respectively.

PSNR values of each sampling ratio decrease rather gradually with lowering sampling ratio down to 5%, which is followed by a relatively rapid decrease for the sampling ratios below 5%. Based on this information, PSNR can be a guideline for selecting optimum electron dose (i.e. sampling ratio).

Table 1. Results of the quantification of the particle size and number from the conventional STEM image (here, the reference) and the reconstructed images with 20%, 10%, 5%, and 3% sampling.

	Reference	20%	10%	5%	3%
Number of particles	150	150	150	149	144
Average diameter (nm)	12.43	12.43	12.44	12.14	11.78

As previously reported, a lower bound of sampling ratio depends on the complexity and fine details (e.g. grain boundaries, location of atomic columns) of the specimen under investigation [17]. That is, the optimum sampling ratio for the sparse acquisition is not invariant of materials. Therefore, the random sparse acquisition STEM should be preceded by a PSNR study to determine the optimum sampling ratio for each specific material system. However, the upper bound of the sampling ratio optimization is physically limited by the beam sensitivity and the damage threshold of a specific material. In this regard, the optimization process should be done below the maximum sampling ratio below which no significant electron beam damage is observed. Based on the calculated PSNR for Au on carbon film shown in figure 6, it can be inferred that 5% sampling is applicable to typical nanoparticle samples.

So far, our experimental results have demonstrated that the random sparse-scan approach in STEM can generate high quality STEM images even with a low sampling ratio, such as 5%, and this demonstrates the high potential of the sparse STEM acquisition for a low dose imaging. However, there are currently practical challenges and limitations for this technique to be used for high-resolution STEM imaging and/or low dose imaging due to the inherent instrumental limitations in widely used conventional microscopes:

First, the electron emission from the electron gun is continuous and turning on/off the emission is not freely controllable. Because of this, electron dose keeps accumulating during the time interval between the probe re-positionings throughout the random sparse-scan. To minimize or effectively reduce the detrimental electron exposures, an electrostatic electron deflector can be added as an additional hardware in STEM. The electrostatic electron deflector can be synchronously operated with the random sparse-scan to deflect the electron beam out from the optic axis of the STEM instrument as demonstrated by Reed *et al* for the movie-mode dynamic TEM (DTEM) [33]. Second, both hardware and software of the widely used conventional STEMs are optimized for a line-by-line or a pixel-by-pixel scan (i.e. raster scan) and it is currently unrealizable to shorten the intervals between the random sparse-scans to be negligible in comparison to the dwell time using the available software–hardware architecture in conventional STEM instruments. Due to this instrumentational limit, repositioning of the electron probe during the random sparse scan causes longer times to acquire an image than the time required to acquire an image by conventional raster scan. Moreover, since the 'scan-skip-scan' type of probe control in the sparse-scan is more complicated than the continuous

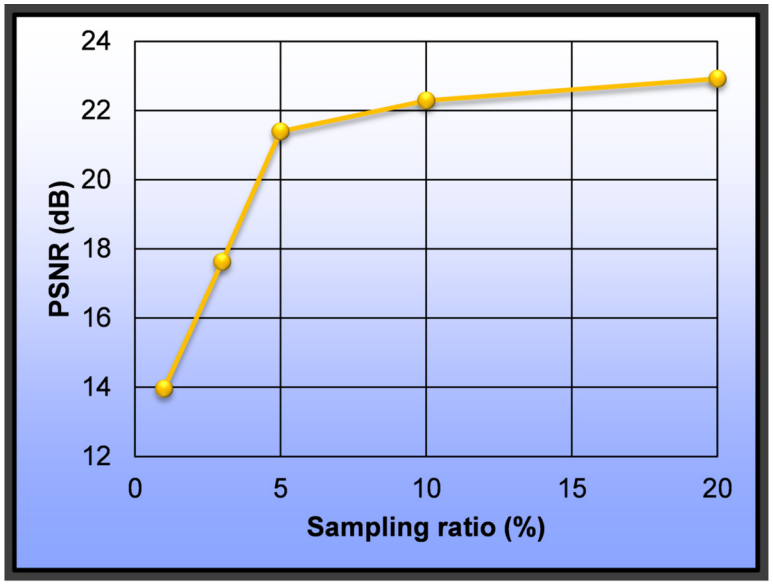

Figure 6. Variation of the peak signal-to-noise ratio (PSNR) of the reconstructed images with varying sampling ratios.

raster scan, it inevitably takes longer time than conventional imaging. As a result, it requires drift correction especially for high sampling ratios (drift correction is implemented in the *SSTEMbot* to alleviate the potential of sample drifting due to scan-skip-scan type of probe control). Therefore, the longer acquisition times, mainly caused by the repositioning of the electron probe during the intervals, may potentially increase an electron dose due to the continuous emission from the gun. In this regard, developing a sparse and fast image collection scheme, which is implementable on a conventional scan-coil control system, is crucial to achieve its full potential in a low dose imaging. Kovarik *et al* demonstrated that a continuous lateral scan with a random vertical perturbation, which is analogous to the raster scan can improve the image collection speed, although their method requires the custom-build external control hardware for the scan coils [34].

4. Conclusions

In this paper, we implemented a random sparse acquisition STEM technique on a widely used FEI Titan 80-300 S/TEM microscope. The random sparse-scan was performed by the *SSTEMbot* application, employing a custom automation interface supported by TIA. Sparse images of Au on carbon film with varying sampling ratios were reconstructed by the MBIR algorithm, so called the Plug-and-Play priors. The results of the reconstruction from the sparse images of down to 5% were consistent with that of the conventionally acquired image. These results demonstrate the significant potential of the sparse acquisition STEM for low-dose imaging of the beam sensitive materials. However, the instrumental limitations in current conventional microscopes, such as the continuous electron beam emission and the time delays between the repositioning of the electron probe due to the internal electronic delays, limits the full utilization of this innovative technique in nanomaterials research. However, modifications of the conventional STEMs, such as adding electrostatic electron beam deflectors and faster electronics for the STEM control hardware, and optimization of the image inpainting algorithm used in the reconstruction of the images offers a viable potential solution to achieve low dose and high resolution imaging in the sparse acquisition STEM.

Competing interests

The authors declare that they have no competing interests.

References

[1] Crewe A V 1966 Scanning electron microscopes: is high resolution possible? *Science* **154** 729
[2] Crewe A V 1968 A high-resolution scanning transmission electron microscope *J. Appl. Phys.* **39** 5861
[3] Crewe A V and Walls J 1970 A scanning microscope with 5 Å resolution *J. Mol. Biol.* **48** 375
[4] Crewe A V, Wall J and Langmore J 1970 Visibility of single atoms *Science* **168** 1338
[5] Batson P E, Dellby N and Krivanek O L 2002 Sub-ångstrom resolution using aberration corrected electron optics *Nature* **418** 617
[6] Tiemeijer P C, Bischoff M, Freitag M and Kisielowski C 2012 Using a monochromator to improve the resolution in TEM to below 0.5 Å. part I: creating highly coherent monochromated illumination *Ultramicroscopy* **114** 72
[7] Varela M *et al* 2004 Spectroscopic imaging of single atoms within a bulk solid *Phys. Rev. Lett.* **92** 95502
[8] Bosman M, Keast V, García-Muñoz J, D'Alfonso A, Findlay S and Allen L 2007 Two-dimensional mapping of chemical information at atomic resolution *Phys. Rev. Lett.* **99** 86102
[9] Sang X and Lebeau J M 2014 Revolving scanning transmission electron microscopy: correcting sample drift distortion without prior knowledge *Ultramicroscopy* **138** 28
[10] Buban J P, Ramasse Q, Gipson B, Browning N D and Stahlberg H 2010 High-resolution low-dose scanning transmission electron microscopy *J. Electron Microsc.* **59** 103
[11] Donoho D L 2006 Compressed sensing *IEEE Trans. Inf. Theory* **52** 1289

[12] Sauer K and Bouman C 1993 A local update strategy for iterative reconstruction from projections *IEEE Trans. Signal Process.* **41** 534
[13] Leary R, Saghi Z, Midgley P A and Holland D J 2013 Compressed sensing electron tomography *Ultramicroscopy* **131** 70
[14] Saghi Z, Holland D J, Leary R, Falqui A, Bertoni G, Sederman A J, Gladden L F and Midgley P A 2011 Three-dimensional morphology of iron oxide nanoparticles with reactive concave surfaces. a compressed sensing-electron tomography (CS-ET) approach *Nano Lett.* **11** 4666
[15] Saghi Z *et al* 2015 Reduced-dose and high-speed acquisition strategies for multi-dimensional electron microscopy *Adv. Struct. Chem. Imaging* **1** 7
[16] Binev P, Dahmen W, Devore R, Lamby P, Savu D and Sharpley R 2012 Compressed sensing and electron microscopy *Modeling Nanoscale Imaging in Electron Microscopy* (Boston, MA: Springer) (doi: 10.1007/978-1-4614-2191-7_4)
[17] Stevens A, Yang H, Carin L, Arslan I and Browning N D 2013 The potential for Bayesian compressive sensing to significantly reduce electron dose in high-resolution STEM images *Microscopy* **63** 41
[18] Béché A, Goris B, Freitag B and Verbeeck J 2016 Development of a fast electromagnetic beam blanker for compressed sensing in scanning transmission electron microscopy *Appl. Phys. Lett.* **108** 093103
[19] Venkatakrishnan S V, Bouman C A and Wohlberg B 2013 Plug-and-Play priors for model based reconstruction *IEEE Global Conf. on Signal and Information Processing* p 945
[20] Yu Z, Thibault J-B, Bouman C A, Sauer K D and Hsieh J 2011 Fast model-based x-Ray CT reconstruction using spatially nonhomogeneous ICD optimization *IEEE Trans. Image Process.* **20** 161
[21] Sauer K and Bouman C 1992 Bayesian estimation of transmission tomograms using segmentation based optimization *IEEE Trans. Nucl. Sci.* **39** 1144
[22] Fessler J A 1994 Penalized weighted least-squares image reconstruction for positron emission tomography *IEEE Trans. Med. Imaging* **13** 290
[23] Boas D A, Brooks D H, Miller E L, DiMarzio C A, Kilmer M, Gaudette R J and Zhang Q 2001 Imaging the body with diffuse optical tomography *IEEE Signal Process. Mag.* **18** 57
[24] Zhang R, Bouman C A, Thibault J-B and Sauer K D 2013 Gaussian mixture Markov random field for image denoising and reconstruction *IEEE Global Conf. on Signal and Information Processing* p 1089
[25] Milanfar P 2013 A tour of modern image filtering: new insights and methods, both practical and theoretical *IEEE Signal Process. Mag.* **30** 106
[26] Buades A, Coll B and Morel J 2005 A non-local algorithm for image denoising *Comput. Vis. Pattern Recognit.* **2** 60
[27] Aharon M, Elad M and Bruckstein A 2006 *rmK*-SVD: An Algorithm for Designing Overcomplete Dictionaries for Sparse Representation *IEEE Trans. Image Process.* **54** 4311
[28] Hou Y, Zhao C, Yang D and Cheng Y 2011 Comments on "Image denoising by sparse 3-D transform-domain collaborative filtering *IEEE Trans. Image Process.* **20** 268
[29] Chatterjee P and Milanfar P 2012 Patch-based near-optimal image denoising *IEEE Trans. Image Process.* **21** 1635
[30] Boyd S 2010 Distributed optimization and statistical learning via the alternating direction method of multipliers Found. Trends® *Mach. Learn.* **3** 1
[31] Sreehari S, Venkatakrishnan S V, Wohlberg B, Buzzard G, Drummy L F, Simmons J P and Bouman C A 2016 Plug-and-play priors for bright field electron tomography and sparse interpolation *IEEE Trans. Comput. Imaging* **2** 408
[32] Godaliyadda G M D, Buzzard G T and Bouman C A 2014 A model-based framework for fast dynamic image sampling *IEEE Int. Conf. on Acoustics Speech and Signal Processing (Florence, Italy, 4–9 May 2014)* pp 1822–6
[33] LaGrange T, Reed B W, DeHope W, Shuttlesworth R and Huete G 2011 Movie mode dynamic transmission electron microscopy (DTEM): multiple frame movies of transient states in materials with nanosecond time resolution *Microsc. Microanal.* **17** 458
[34] Kovarik L, Stevens A, Liyu A and Browning N D 2016 Implementing an accurate and rapid sparse sampling approach for low-dose atomic resolution STEM imaging *Appl. Phys. Lett.* **109** 164102